

Chapter 3

Co-seismic slip from the July 30, 1995, M_w 8.1 Antofagasta, Chile, earthquake as constrained by InSAR and GPS observations

Published by Blackwell Publishing Ltd. in *Geophysical Journal International* by M. E. Pritchard, M. Simons, P. A. Rosen, S. Hensley and F. H. Webb, **150**: 362-376, 2002.

Abstract

We analyze radar interferometric and GPS observations of the displacement field from the July 30, 1995, M_w 8.1 Antofagasta, Chile, earthquake and invert for the distribution of slip along the co-seismic fault plane. Using a fixed fault geometry, we compare the use of singular value decomposition and constrained linear inversion in inversions for the slip distribution and find that the latter approach provides better resolution and is more physically reasonable. Separate inversions using only GPS data, only InSAR data from descending orbits, and InSAR data from both ascending and descending orbits without the GPS data illustrate the complimentary nature of GPS and the presently available InSAR data. The GPS data resolve slip near GPS benchmarks well, while the InSAR provides greater spatial sampling. The combination of ascending and descending InSAR data improves the ability of InSAR to resolve the slip model, thereby emphasizing the need to acquire this data for future earthquakes. The rake, distribution of slip, and seismic moment of our preferred model are generally consistent with previous seismic and geodetic inversions, although significant differences do exist. GPS data projected in the radar line-of-sight (LOS) and corresponding InSAR pixels have a root mean square (RMS) difference of about 3 cm. Comparison of our predictions of vertical displacement and observed uplift from coralline algae have an RMS of 10 cm. Our inversion and previous results reveal that the location of slip might be influenced by the 1987 M_w 7.5 event. Our analysis further reveals that the 1995 slip distribution was affected by a 1988 M_w 7.2 event, and might have influenced a 1998 M_w 7.0 earthquake which occurred downdip of the 1995 rupture. Our slip inversion reveals a potential change in mechanism in the southern portion of the rupture, consistent with seismic results. Predictions of the satellite

LOS displacement from a seismic inversion and a joint seismic/GPS inversion do not compare favorably with the InSAR observations.

3.1 Introduction

A primary goal of earthquake geodesy is to invert observations of surface displacement for the distribution of slip along the fault plane (e.g., *Segall and Harris*, 1987; *Du et al.*, 1992; *Sagiya and Thatcher*, 1999). However, there are both fundamental and practical limitations to resolving slip associated with subduction earthquakes. All geodetic observations are made 10's of km from the fault plane, and the largest surface deformation is off-shore and inaccessible to measurement (e.g., *Sagiya and Thatcher*, 1999). Therefore, any estimation of the slip distribution must include an analysis of our ability to resolve this slip (e.g., *Du et al.*, 1992; *Árnadóttir and Segall*, 1994; *Thatcher et al.*, 1997; *Sagiya and Thatcher*, 1999). In practice, observations of surface deformation are rather sparse (for example, at GPS benchmarks or along leveling lines), fundamentally limiting the ability to well resolve slip along the fault plane. Interferometric Synthetic Aperture Radar (InSAR) has the potential to overcome the practical limitation of poor spatial sampling by densely and accurately measuring the surface deformation field (for an overview of InSAR methodology, see *Massonnet and Feigl*, 1998; *Rosen et al.*, 2000). The limitation of using only on-shore data is not eliminated by InSAR, but can be reduced by using tsunami waveform data (e.g., *Satake*, 1993), not considered here). In this paper, we invert InSAR and GPS measurements to determine the slip distribution from the M_w 8.1, July 30, 1995, Antofagasta, Chile, earthquake (see Figure 3.1).

3.2 Previous work

The July 30, 1995, M_w 8.1 earthquake began at about 5:11 am (GMT) beneath the Mejillones Peninsula (*Monfret et al.*, 1995, NEIC), and ruptured unilaterally to the southwest (*Delouis et al.*, 1997; *Ihmlé and Ruegg*, 1997; *Gouget et al.*, 1998; *Carlo et al.*, 1999). A mild tsunami of 2.8 m beached in Antofagasta (*Ramirez et al.*, 1997). The discrepancy between the moment magnitude, M_w 8.1, and the surface-wave magnitude, M_s 7.3, is attributed to significant moment release at long periods

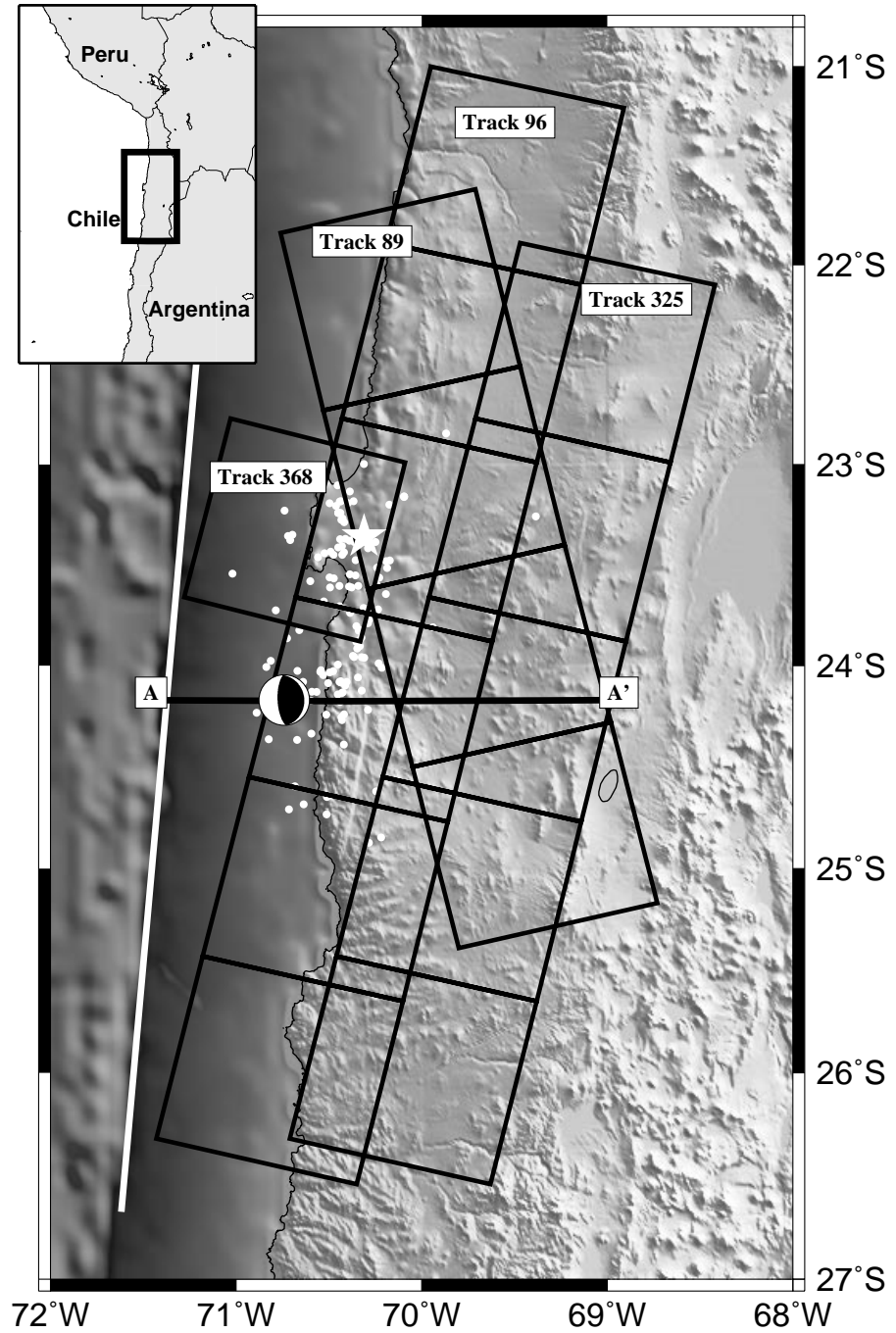


Figure 3.1: Reference map of our study area in northern Chile corresponding to the black box in the upper left inset map. The Harvard CMT solution for the mainshock is indicated, and the white star shows the location from the NEIC catalog. Aftershocks with $M_w > 2.5$ are indicated by white dots (Husen *et al.*, 1999). The white line indicates the surface trace of the fault along the subduction zone (at the bottom of the oceanic trench). Black squares outline the frames of ERS radar data used in this study. Profile A-A' is shown in Figure 3.7.

and suggests that the event was a slow earthquake (*Ruegg et al.*, 1996; *Delouis et al.*, 1997; *Carlo et al.*, 1999). The focal mechanism p-axis is nearly coincident with the plate convergence direction of NUVEL-1A (*DeMets et al.*, 1994), and is inconsistent with significant slip partitioning at this location (*Ruegg et al.*, 1996). Figure 3.2 shows the relation between the 1995 earthquake and other large earthquakes in northern Chile.

Several studies consider both seismic and geodetic data from the earthquake (*Ruegg et al.*, 1996; *Delouis et al.*, 1997; *Ihmlé and Ruegg*, 1997), although only *Ihmlé and Ruegg* (1997) did a joint seismic and geodetic inversion for fault slip. *Delouis et al.* (1997) found good agreement in a visual comparison between a finite fault model based on teleseismic body-waves with observations made by *Ortlieb et al.* (1995) of coastal co-seismic uplift. *Carlo et al.* (1999) used teleseismic body and long period surface waves to invert for the source time function. *Reigber et al.* (1997) published co-seismic interferograms of the 1995 earthquake covering a fraction of the deformation field near the Mejillones Peninsula. They found that the measured displacements were similar (difference less than 2 cm) to co-seismic vector displacements from 7 GPS stations when projected in the radar line-of-sight (LOS). The GPS stations are part of the SAGA (South American Geodynamic Activities) project operated by the GeoForschungsZentrum Potsdam (GFZ). *Klotz et al.* (1999) used the co-seismic displacements from 70 GPS stations of the SAGA network to invert for the co-seismic slip distribution. *Sobiesiak* (2000) found a correlation between the b-value of the aftershock distribution from the 1995 earthquake and areas of high slip, perhaps providing a map of structural heterogeneities on the fault plane.

Although the Antofagasta earthquake has been extensively studied, several issues remain. *Carlo et al.* (1999) observed that there is no obvious relation between the distribution of co-seismic slip and the location of aftershocks, but suggested that a better resolved two-dimensional slip map might reveal such a dependence. The primary goal of this study is a better resolved two-dimensional slip map that can be used in future models of post-seismic deformation and to study interaction between the 1995 earthquake and events in 1987, 1988, and 1998. *Ihmlé and Ruegg* (1997)

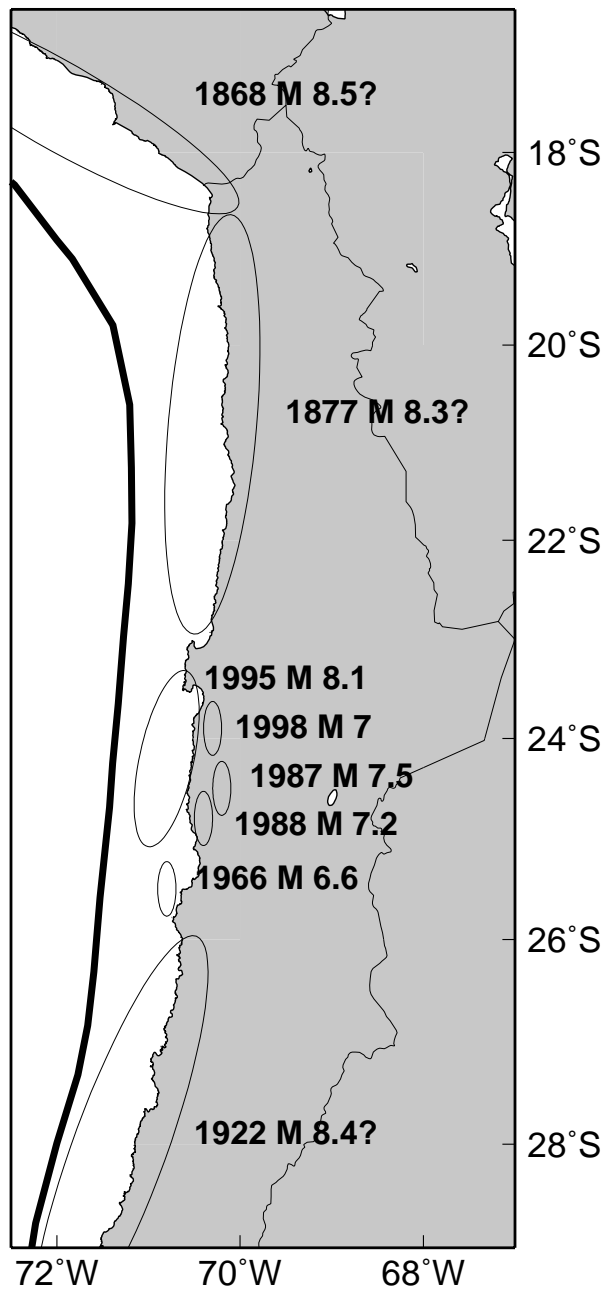


Figure 3.2: Estimated rupture zones for earthquakes in northern Chile with dates and approximate moments (*Comte and Pardo*, 1991; *Tichelaar and Ruff*, 1991; *Ruegg et al.*, 1996; *Delouis et al.*, 1997; *Carlo et al.*, 1999). There is considerable uncertainty in the rupture areas for all but the 1995 event. In particular, the 1877 rupture zone could extend south into the 1995 rupture area (e.g., *Lay et al.*, 1982), but probably does not (*Kausel and Campos*, 1992).

claim that in order to fit the vertical component of GPS displacements, a change in dip of the subduction interface from 20° to 25° under the coast was required. Such a change in dip is not seen by other seismic studies (*Delouis et al.*, 1996), although it is questionable whether the change in dip would be observed since it is below the resolution supported by those studies (*Ihmlé and Ruegg*, 1997). A change in dip of the subduction interface was suggested by *Armijo and Thiele* (1990) as a possible cause of coastal uplift, and so another goal of this work is to determine whether the geodetic data require such a change in dip.

3.3 Data used

We use ERS-1 and ERS-2 radar images acquired between 1992 and 1997 (Figure 3.1). We use radar data from four satellite tracks – three descending (tracks 96, 325, and 368) and one ascending (track 89). Radar interferometry measures the change in path length in the radar LOS between observations. Data from the different viewing angles of the different satellite tracks provide multiple components of deformation. Interferograms include the effects of differences in satellite viewing geometry, topography, tropospheric and ionospheric changes, and deformation of the Earth's surface (e.g., *Massonnet and Feigl*, 1998; *Rosen et al.*, 2000). We process the SAR data using the Caltech/JPL repeat-orbit interferometry package, ROI_PAC. In the processing, we use orbital information, accurate to about 20 cm, provided by the Delft Institute for Earth-Oriented Space Research in the Netherlands (*Scharroo et al.*, 1998). We remove the topographic signal with both the 2-pass approach where a pre-existing digital elevation model (DEM) is used, and the 4-pass approach which uses ERS-1/2 tandem data (separated in time by one day). Existing DEMs in our study area have large gaps and poor accuracy in areas where they do exist. Therefore, we constructed a DEM of our area by mosaicing six pairs of tandem data from the four satellite tracks to use both in the 2-pass approach and in the geocoding process. However, even our DEM has artifacts and cannot be used to remove topography when the perpendicular baseline is large, so for those interferograms we use the 4-pass approach.

Northern Chile is an ideal location for the use of InSAR because the lack of rainfall, vegetation, and human cultivation means that there is little non-tectonic change in the surface, even over long time periods. However, atmospheric variations can contaminate the deformation signal, especially near the coast. We minimize atmospheric contamination by using interferograms acquired on several different dates when atmospheric effects should be uncorrelated. From a geophysical perspective, northern Chile is a favorable study area because the coast is closer to the trench than in many other subduction zones, so that more of the deformation signal is on land. Furthermore, the Mejillones Peninsula protrudes trenchward and allows us to observe part of the co-seismic uplift.

We had to address a number of problems with the raw data that otherwise would have made it impossible to obtain acceptable slip distributions. First, some of the raw data was corrupted with missing lines or, less commonly, unnecessary lines were added that caused a loss of coherence in the interferograms (as evidenced by horizontal streaks in Figure 7 of *Reigber et al.* (1997) and Figure 3.3). The line counter within the raw data itself is often insufficient to solve this problem, so we used the onboard clock information to find the missing lines. Unfortunately the clock records have insufficient temporal precision so that many lines have the same “time.”

Even with the corrupted data fixed, radar data was not collected during most passes over the area, so that all interferograms include deformation from multiple sources. Temporal coverage for the ascending track is especially poor. Only two ascending interferograms can be made that include co-seismic deformation, one of which has severe short wavelength distortion (of probable ionospheric origin, see Figure 3.4) rendering it useless, and the other spans a time period of 4.5 years. Even when the data was acquired, not all of the frames of a given satellite track were collected, so that maps of the deformation over some time intervals are shorter in along-track extent than others (Figure 3.5). Additionally, we found that the pulse repetition frequency (PRF) can vary between acquisitions and that the baseline has a second order variation that becomes important when many frames are concatenated. In the cases where precise ERS orbits were not available, we estimated the baseline

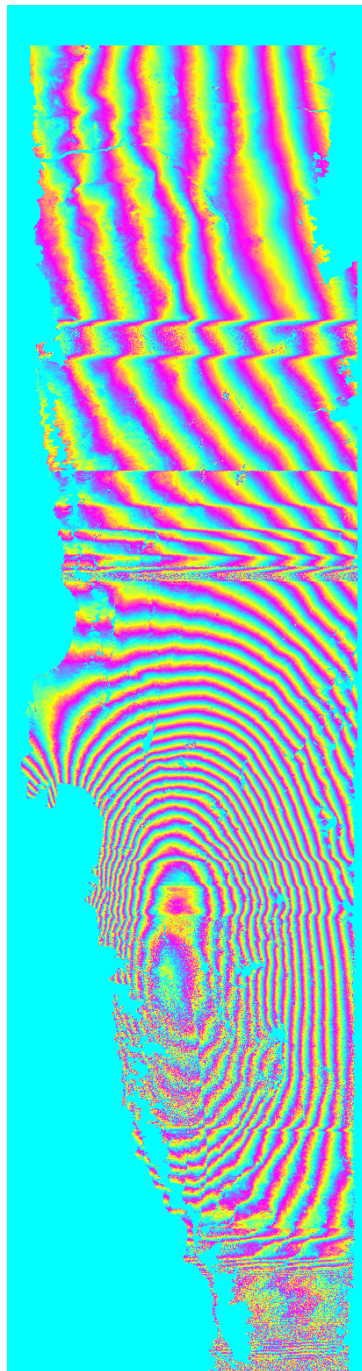


Figure 3.3: Wrapped interferogram from track 96 spanning 10/9/1995-5/8/1992 in radar coordinates (range is horizontal and azimuth is vertical) showing the effects of missing lines upon the phase. A portion of this interferogram was originally shown by *Simons et al.* (1996) and this image was made by *Pritchard et al.* (1998). The regions with missing (or added) lines are visible because the fringes are offset where they begin and end. Within the regions with missing lines, the fringe visibility and coherence are reduced. The same interferogram is shown unwrapped in Figure 3.5 with the missing lines corrected and in geographic coordinates.

directly from the data by removing a model of deformation and then finding the best fit orbital parameters that minimized the residual between the interferogram (with the model removed) and a synthetic interferogram made with a DEM (*Rosen et al.*, 1996). To minimize possible short wavelength atmospheric effects when estimating the baselines in this way, we use as many frames of radar data as possible in each satellite track (*Fujiwara et al.*, 1998).

Track	Pre-seismic image	Post-seismic image	B_{\perp} (m)	B_{\perp} topo pair (m)
96	5 May 1992	9 Oct. 1995	50	120
96	16 Apr. 1995	8 Oct. 1995	110	120
96	16 Apr. 1995	30 Jul. 1995	200	120
96	16 Apr. 1995	13 Oct. 1997	20	120
325	24 May 1992	15 Aug. 1995	80	100
325	24 May 1992	19 Sep. 1995	40	100
325	11 Jul. 1995	19 Sep. 1995	130	100
89	28 May 1993	12 Oct. 1997	150	300
368	14 Jul. 1995	18 Aug. 1995	50	300

Table 3.1: Data from three descending satellite tracks (96, 325, and 368) and one ascending track (89) used in inversions for co-seismic slip. B_{\perp} refers to an estimate of the perpendicular baseline at the beginning of each track. For comparison, the GPS data was collected in October and November in both 1993 and 1995 (*Klotz et al.*, 1999).

Figure 3.5 shows four phase unwrapped interferograms with the observed LOS displacements, and Table 3.1 lists the nine interferograms we have used. The InSAR and GPS data contain several years of inter-seismic and several weeks to months of post-seismic deformation, although our examination of pre and post-seismic images indicates that the co-seismic deformation makes up more than 90% of the signal. For example, we see 15 fringes in the co-seismic interferograms and less than one fringe in post-seismic interferograms (see Chapter 4). To remove possible inter-seismic and post-seismic deformation, we estimate the best fitting quadratic ramps in space for each component of the displacement field (*i.e.*, for each interferogram and each component of GPS deformation) in addition to the fault slip model parameters. We have used a quadratic instead of a linear ramp to approximate the spatial shape of the

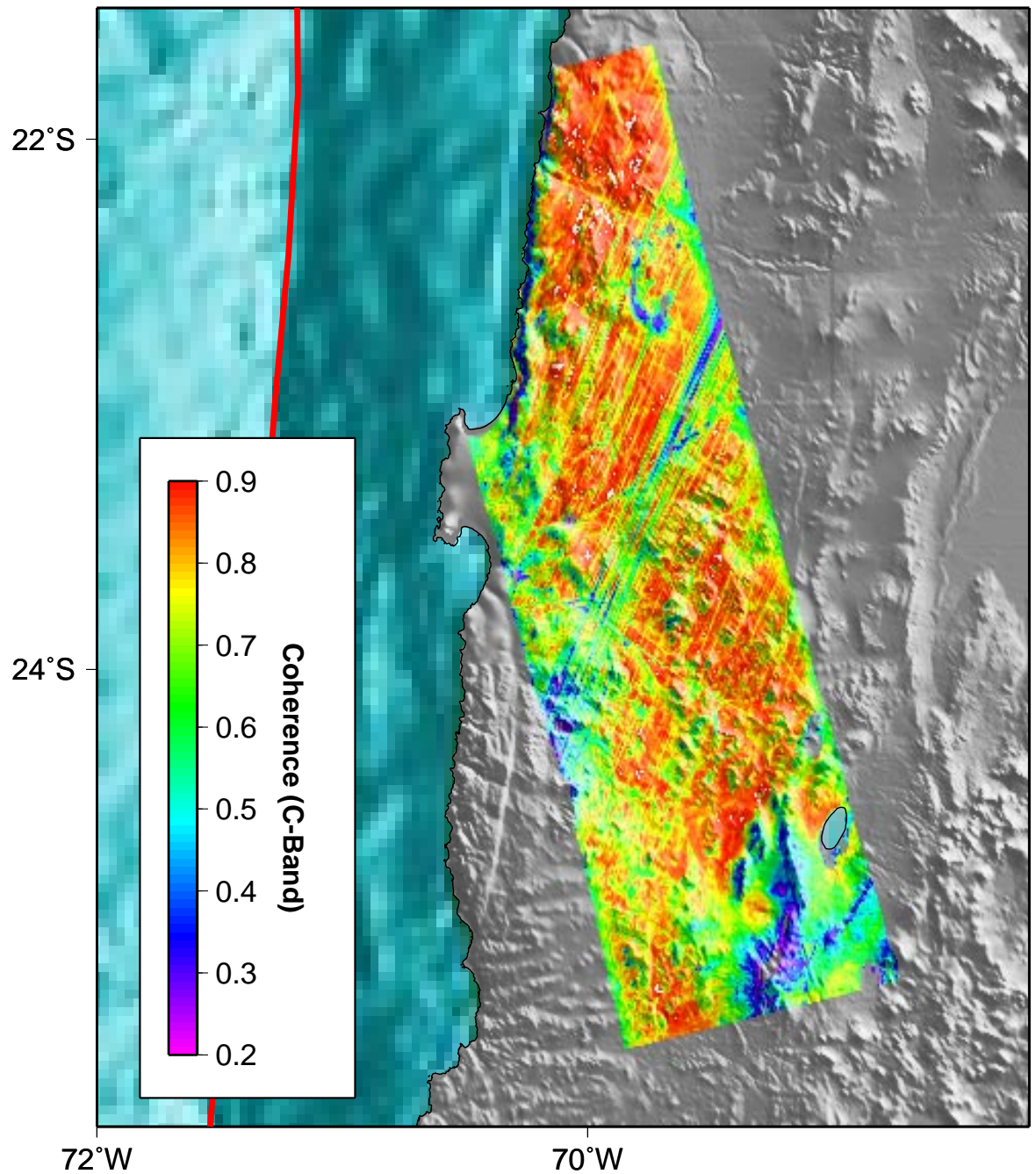


Figure 3.4: Coherence image from ascending orbital track 89 (spans 4/23/1993-10/13/1997) showing streaks oriented southwest-northeast (about 20° from north) that render the phase in the interferogram unusable. Streaks are not observed in another image (spanning 5/28/1993-10/12/1997, see Figure 3.5) and are more subtle in another (spanning 10/13/1997-10/12/1997). All images were acquired around 03:30 GMT. We hypothesize that the artifacts are caused by plasma irregularities in the F layer of the ionosphere (D. Hysell, personal communication, 2003).

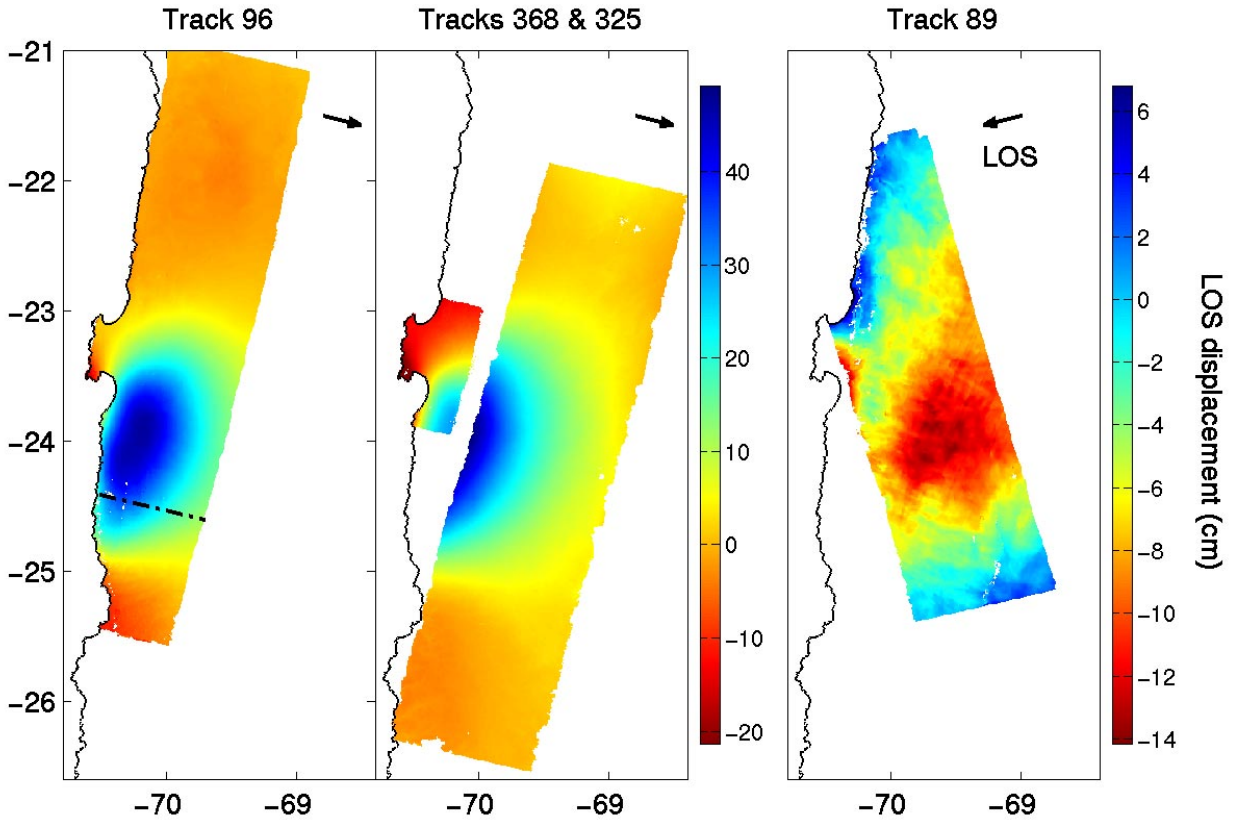


Figure 3.5: Unwrapped co-seismic interferograms used to invert for co-seismic slip from descending satellite tracks 96, 325, 368, and ascending track 89. Color scale refers to change in the radar LOS direction in cm over the timescales indicated in Table 3.1. Black arrows show the LOS vector from the ground to the satellite projected onto the ground. We show the interferogram from track 96 spanning May 8, 1992 to October 9, 1995, because the other acquisitions do not span all available frames (the dotted black line shows where they end). For track 325, all interferograms have the same length and the interferogram spanning May 24, 1995 and September 19, 1995 is shown for reference. The maximum observed LOS displacement is about 50 cm away from the satellite in the descending scenes where there is co-seismic subsidence and westward horizontal displacement, both of which increase the LOS distance. The LOS displacements in the ascending interferogram are smaller (maximum of about 10 cm) since the westward horizontal motions correspond to a decrease in LOS distance while subsidence increases the LOS distance, thereby partially cancelling each other.

inter-seismic strain that might decrease in a quasi-quadratic manner away from the trench (e.g., *Savage*, 1983) and because InSAR orbital errors can also be quadratic in shape (e.g., *Zebker et al.*, 1994).

Each of the satellite tracks used in this study have of order 10^8 pixels at full resolution, and even when transformed from radar to geographic coordinates using a low resolution DEM there are of order 10^7 pixels. This number is currently impractical to include in an inversion, and as we will show, unnecessary for slip distribution inversion from large, relatively deep events. We use a uniform sampling by simply averaging nearby pixels together (commonly called “looking down”), so that the total number of displacement measurements is manageable. Because the surface deformation pattern from the Antofagasta earthquake is smooth, averaging many pixels together does not lose any of the details of the deformation signal. This approach will fail in areas near where a fault ruptures the surface or the phase gradient is extremely high (like at the Landers and Hector Mine, California earthquakes). To ensure that no information is lost by looking down the interferograms, we have estimated model parameters at different pixel resolutions and then computed the residual for all models at a high resolution (300 m pixels). Figure 3.6 shows a comparison between the residuals from models calculated at 300 m/pixel and 2.5 km/pixel. The features in each residual are very similar and the RMS residuals are within 0.6 cm. For the rest of the inversions discussed in this paper, we use the InSAR data with a spacing of 2.5 km, combined with the 65 GPS stations in the SAGA array (*Klotz et al.*, 1999) totaling 5.6×10^4 observations.

3.4 Data inversion

We fix the geometry of the fault plane using a quadratic function constrained by the location of the trench (from BOUND.90, compiled by Peter Sloss, unpublished) and the distribution of aftershocks (*Husen et al.*, 1999). The surface is discretized into fault patches as shown in cross-section in Figure 3.7 and map view in Figure 3.8. The dip of our fault patches varies between 20° and 24° , consistent with the distribution

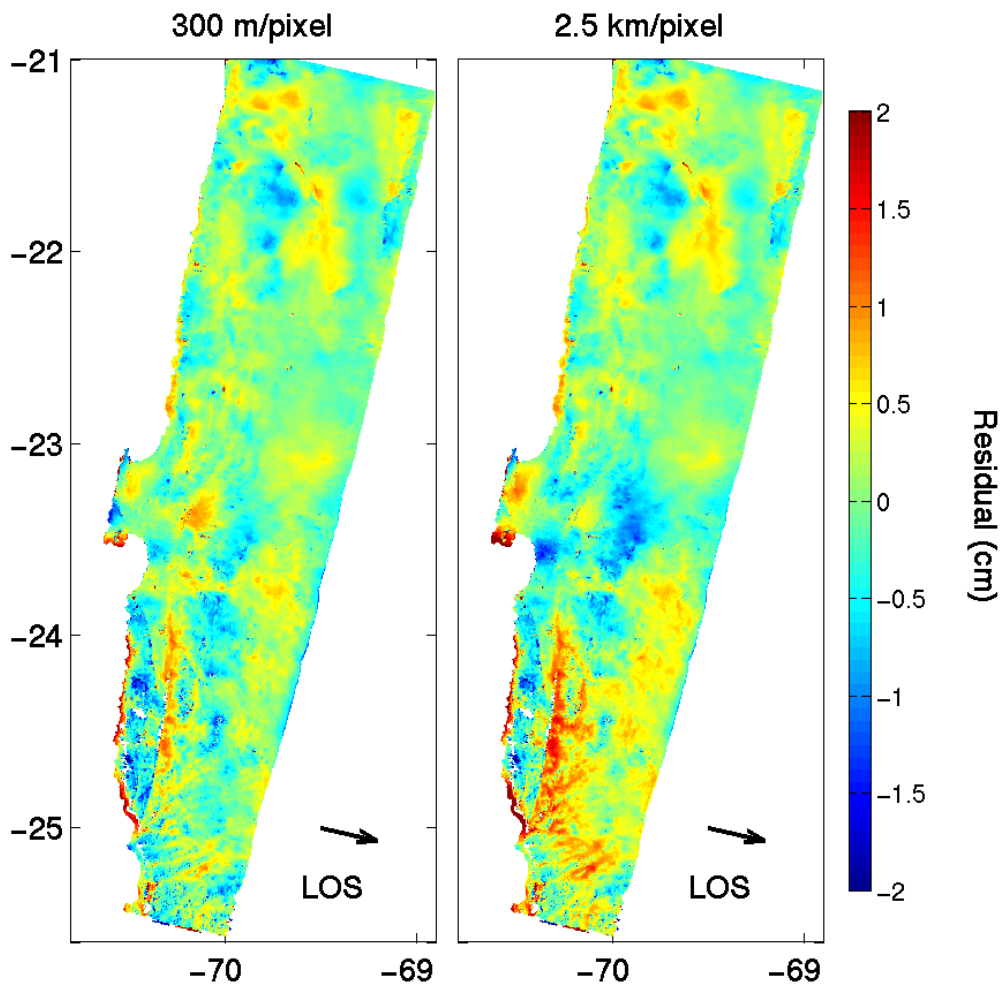


Figure 3.6: Residuals from models generated at different pixel spacings from track 96. The data used to calculate the residual is the same – 300 m/pixel. The RMS for model calculated at 2.5 km/pixel is 0.46 cm and for the model calculated 300 m/pixel is 0.40 cm.

of seismicity, 17° - 18° (*Comte et al.*, 1994; *Delouis et al.*, 1996), calculations of the dip of the 1995 earthquake rupture plane, 15° - 24° (*Ruegg et al.*, 1996; *Ortlieb et al.*, 1996; *Delouis et al.*, 1997; *Ihmlé and Ruegg*, 1997; *Klotz et al.*, 1999; *Carlo et al.*, 1999), and seismic refraction experiments, 9° - 25° (*Patzwahl et al.*, 1999). By fixing the geometry, the inversion for slip becomes linear and is given by the equation $Gm = d$, where m is a vector of the strike-slip and dip-slip components of slip on each patch, d is the vector of displacement observations, and G is the matrix of Green's functions for each fault patch computed using an isotropic elastic half-space model (*Okada*, 1985). We augment this linear system to include coefficients of a quadratic ramp in space for each component of GPS deformation and each interferogram. The fault patches are not all the same size, and we select the size of each patch to maximize model resolution as discussed below. Each side of $Gm = d$ is multiplied by a weight matrix $P_{ij} = \delta_{ij}\sigma_j^{-1}$ where σ_j is the error on the i th datum (e.g., *Harris and Segall*, 1987). We use the error on each component of the GPS measurements from *Klotz et al.* (1999). The errors on the InSAR measurements are not well constrained, but we assume an uncorrelated error of 1 cm on each radar pixel in each track.

We compare results from two methods: truncated singular value decomposition (SVD) (e.g., *Menke*, 1989; *Press et al.*, 1994) and a least-squares constrained linear inversion (CLS). The constrained linear inversion (also called the iterative linear least squares inversion) is part of the MATLAB Optimization Toolbox and based on the work of *Gill et al.* (1981) and *Coleman and Li* (1996). We constrain the dip-slip component to only allow reverse faulting and the strike-slip component to be right-lateral, consistent with the plate convergence direction and previous estimates of the mechanism of the 1995 event. On the other hand, the SVD inversion is unconstrained, which will reduce the model resolution (e.g., *Du et al.*, 1992). However, care must be taken when estimating the truncation value p , because of the well known tradeoff between model variance and data misfit (e.g., *Menke*, 1989). For the SVD inversion, model resolution is given by $R = V_p V'_p$, (e.g., *Menke*, 1989), where V_p is the reduced set of model space eigenvectors. To determine the model resolution when using CLS, we generate synthetic data by putting a unit of slip on each component of slip on each

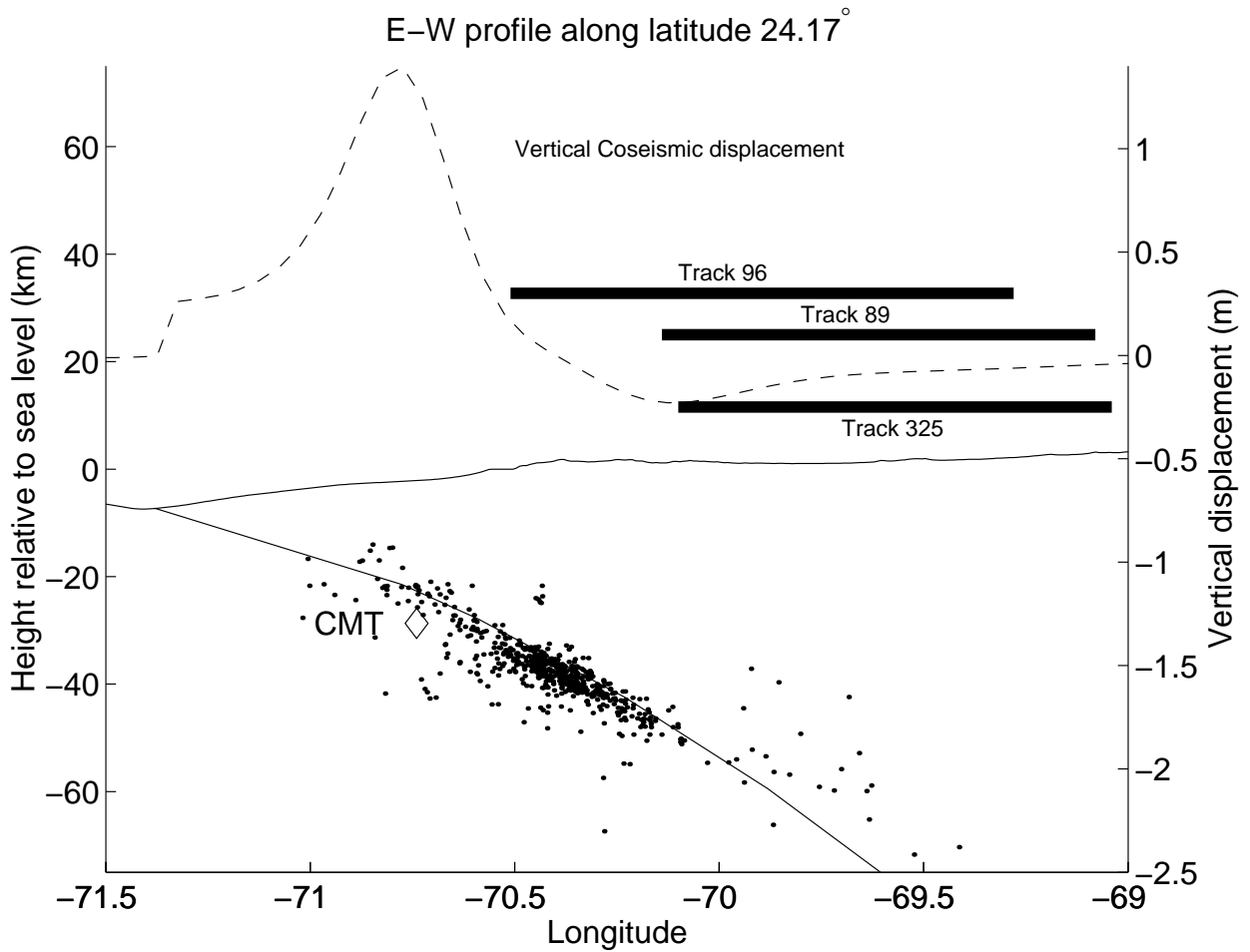


Figure 3.7: Profile along A-A' from Figure 3.1. The dashed line shows a profile of the vertical co-seismic displacement from our model prediction. The dots show all of the aftershocks taken from (*Husen et al.*, 1999) – not just those along the profile. The black line shows the parameterization of the fault plane used in the co-seismic slip inversions. The horizontal thick black lines show the width of the satellite tracks along this profile. The nearly horizontal thin black line shows the topography in the ocean and on land. The Harvard CMT location is shown as a diamond labeled “CMT.”

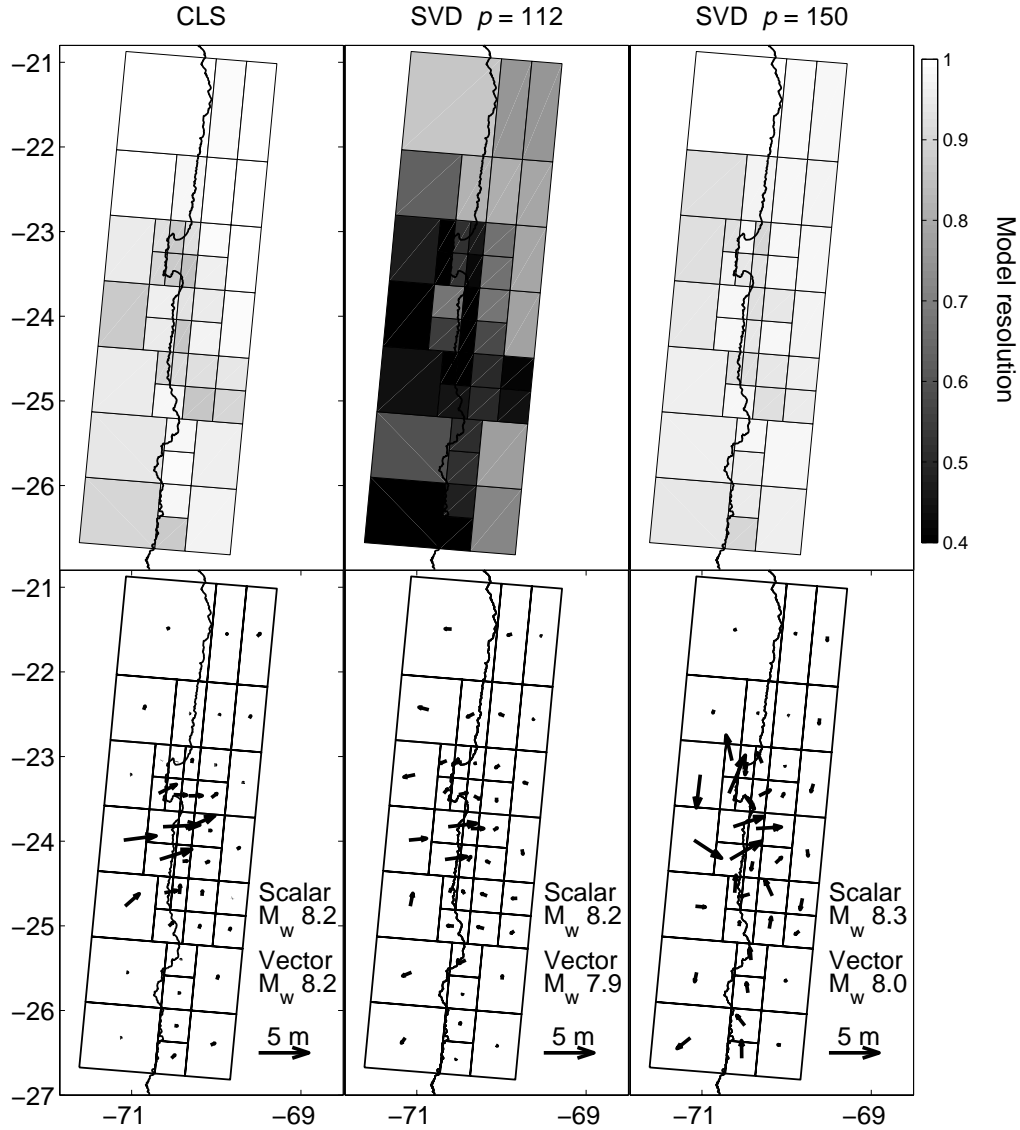


Figure 3.8: Comparison of model resolution and slip distribution from singular value decomposition (SVD) and constrained least squares (CLS). The patch size was determined to optimize CLS resolution (see text for details). The model resolution and slip distribution for the SVD inversion depends on the number of singular values used. We prefer to truncate at 112 singular values, because keeping more singular values does not significantly reduce the RMS residual, see Figure 3.9. However, to more directly compare the SVD and CLS inversions, we also show results from an SVD inversion truncated at a singular value (150) that gives the same mean model resolution as the CLS inversion. The scalar and vector moments are shown for all inversions (see text).

fault patch one at a time, adding noise, and then inverting the synthetic data for the fault slip. The slip that the inversion places on each patch then corresponds to a row in the model resolution matrix (*Du et al.*, 1992). The quadratic ramp components are constrained to have an effect on the order of a few centimeters across the scene.

As mentioned above, because our geodetic data is limited to be on land, not all of the fault patches are equally well resolved. We define an effective resolution to be: $\overline{R} = \sqrt{\frac{R_d^2 + R_s^2}{2}}$, where R_d is the dip-slip and R_s the strike-slip diagonal component of the model resolution matrix. In an iterative, manual process, we adjust the size of each fault patch so that all of the patches have a CLS resolution above 0.8. The dip-slip component of a patch is generally better resolved than the strike-slip component, but for simplicity we keep strike-slip patches the same size as dip-slip patches. Our final parameterization has 41 patches (with 2 slip components per patch) with 72 parameters for the quadratic ramps (absolute phase offset, linear and quadratic spatial variations for each interferogram and component of GPS deformation), giving a total of 154 parameters. With more than 5.6×10^4 observations and judicious construction of spatially variable sub-faults, the problem is no longer under-determined. This variable patch size approach also provides an easy visual assessment of the spatially-variable model resolution.

3.5 Discussion

Figure 3.8 shows a comparison between the model resolution and slip distribution from the CLS inversion and SVD inversions that are truncated at two different values. Our preferred SVD inversion uses the singular value ($p = 112$) above which the RMS residual was rather constant (*Sagiya and Thatcher*, 1999), (Figure 3.9). The fact that we zero out less than one third of a total of 154 parameters indicates that the majority of parameters are well resolved (*Segall and Harris*, 1987; *Harris and Segall*, 1987). In general, the resolution from the constrained inversion is greater than for the unconstrained inversion (e.g., *Du et al.*, 1992). It is not surprising that the CLS slip model is well resolved since we use it to determine the fault size

parameterization. The direction of slip in the CLS model is consistent from patch to patch and resembles the plate convergence direction and previous inversions of the 1995 mechanism. We find that the zone of aftershocks coincides well with the region of significant slip (Figure 3.10), although, as others have observed, there are aftershocks but little slip in the northern half of the Mejillones Peninsula (e.g., Ruegg *et al.*, 1996). The relatively poorer resolution of the SVD model ($p = 112$) allows some unlikely normal slip and slip well outside the 1995 rupture area. The SVD slip model would have higher resolution if more singular values are used (e.g., $p = 150$, Figure 3.8). However, several model parameters in the inversion with 150 singular values are poorly determined which means that some patches have unrealistic large left-lateral slip. Alternatively, the resolution of the SVD model can be improved by changing the configuration of the fault patches and making some of them larger, but we instead choose to rely on the CLS inversion because it is better able to resolve the fine scale slip features. Fundamentally, the regularization provided by the SVD truncation does not allow for the geophysically reasonable *a priori* bounds on of slip direction, while the CLS approach does. The RMS residual from inversions using all the radar and GPS data for the SVD model ($p = 112$) is 0.96 cm, and for the CLS model is 0.80 cm. Figure 3.11 shows the InSAR residual from the CLS model and Figure 3.12 shows a comparison between the predicted and actual GPS displacements. While Ihmlé and Ruegg (1997) suggest that their GPS dataset requires an abrupt change in slab dip, we find that the residual for the GPS data is effectively the same for models that assume a constant dip of the subduction zone fault (results not shown).

The geodetic moment from our preferred model is 2.4×10^{21} Nm, equivalent to a M_w 8.2, and slightly larger than other estimates (see below). However, a small portion of the slip may represent aseismic, inter-seismic, or post-seismic slip that could not be fit by our quadratic ramp. When we only consider the 12 patches with more than 0.5 m of slip, the moment is 1.6×10^{21} Nm, equivalent to a M_w 8.1 (assuming $\mu = 3.2 \times 10^{10}$ Pa). For comparison, the moment from the SVD model ($p = 112$) is 2.9×10^{21} Nm (M_w 8.2), but is only 1×10^{21} Nm (M_w 7.9) for the same

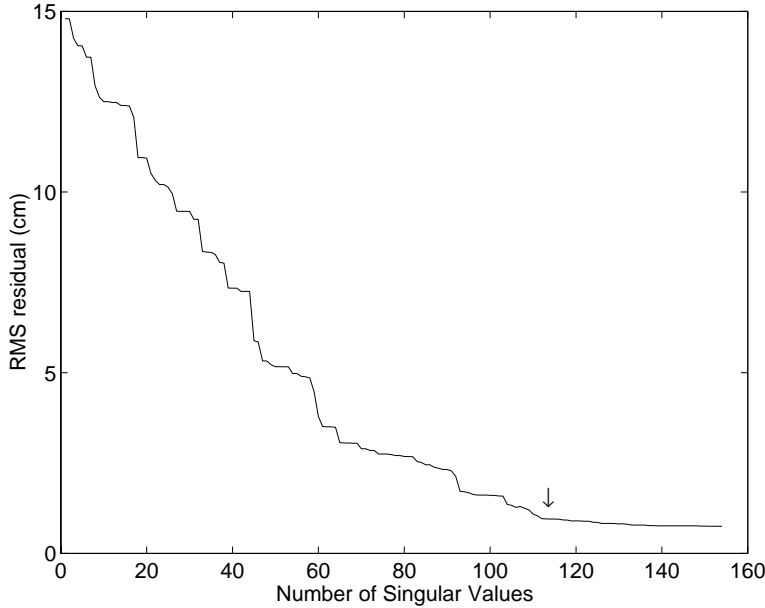


Figure 3.9: RMS residual as a function of the singular value. We truncate singular values beyond 112 (arrow).

12 “co-seismic” patches. The magnitude of slip for this SVD model is less than the CLS model, because of the greater degree of smoothing inherent in the SVD. The moment from the SVD model truncated at 150 is higher – 4.1×10^{21} Nm (M_w 8.3) or 1.5×10^{21} Nm (M_w 8.1) for the same 12 patches. However, the slip distribution in both SVD models is oscillatory, so that when the vector sum of the slip is used in computing the moment for all patches (“Kostrov” summation, *Kostrov*, 1974), the moments are reduced to 8.4×10^{20} Nm (M_w 7.9) and 1.1×10^{21} Nm (M_w 8.0) for the SVD models with 112 and 150 singular values, respectively. The vector sum for the CLS model is only slightly changed to 2.2×10^{21} Nm (M_w 8.2).

3.5.1 Comparison of the slip model with previous work

Our preferred slip model is shown in Figure 3.10 with aftershock locations and epicenters of M_w 7 events that have ruptured near the mainshock during the past 15 years. The seismic moment from our CLS model, considering only the 12 patches with more than 0.5 m of slip (1.6×10^{21} Nm), agrees well with other estimates: seis-

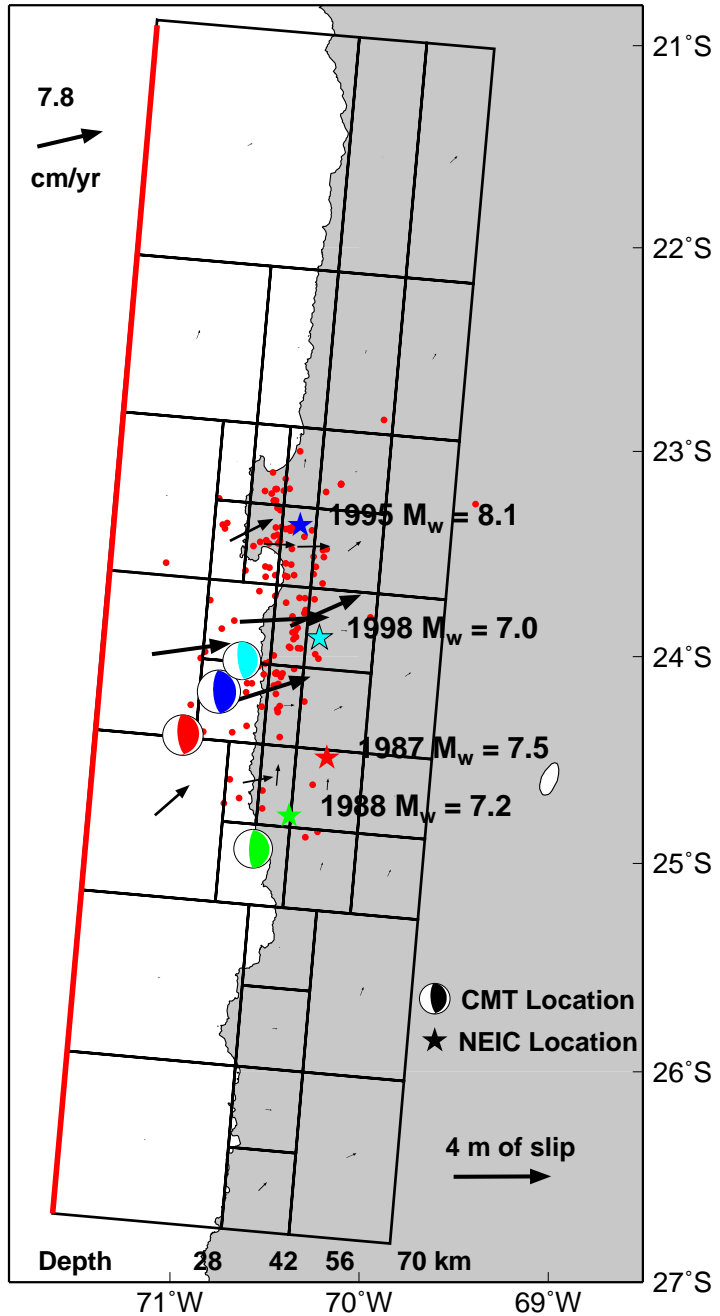


Figure 3.10: Preferred model of co-seismic slip from the 1995 earthquake constrained using GPS from *Klotz et al.* (1999) and 3 descending and 1 ascending tracks of radar data shown by the slip arrows of foot wall. The red dots are aftershocks with $M_w > 2.5$ from the 1995 event (*Husen et al.*, 1999). The arrow in the upper left shows the magnitude and direction of the plate convergence rate (*DeMets et al.*, 1994). The NEIC and Harvard CMT locations for the 1995 and three $M_w 7$ events are shown as stars and moment tensors, respectively. (The NEIC location is where the earthquake began and the CMT location is the center of moment release). Reference depths along the parameterized fault plane are indicated at the bottom of the figure.

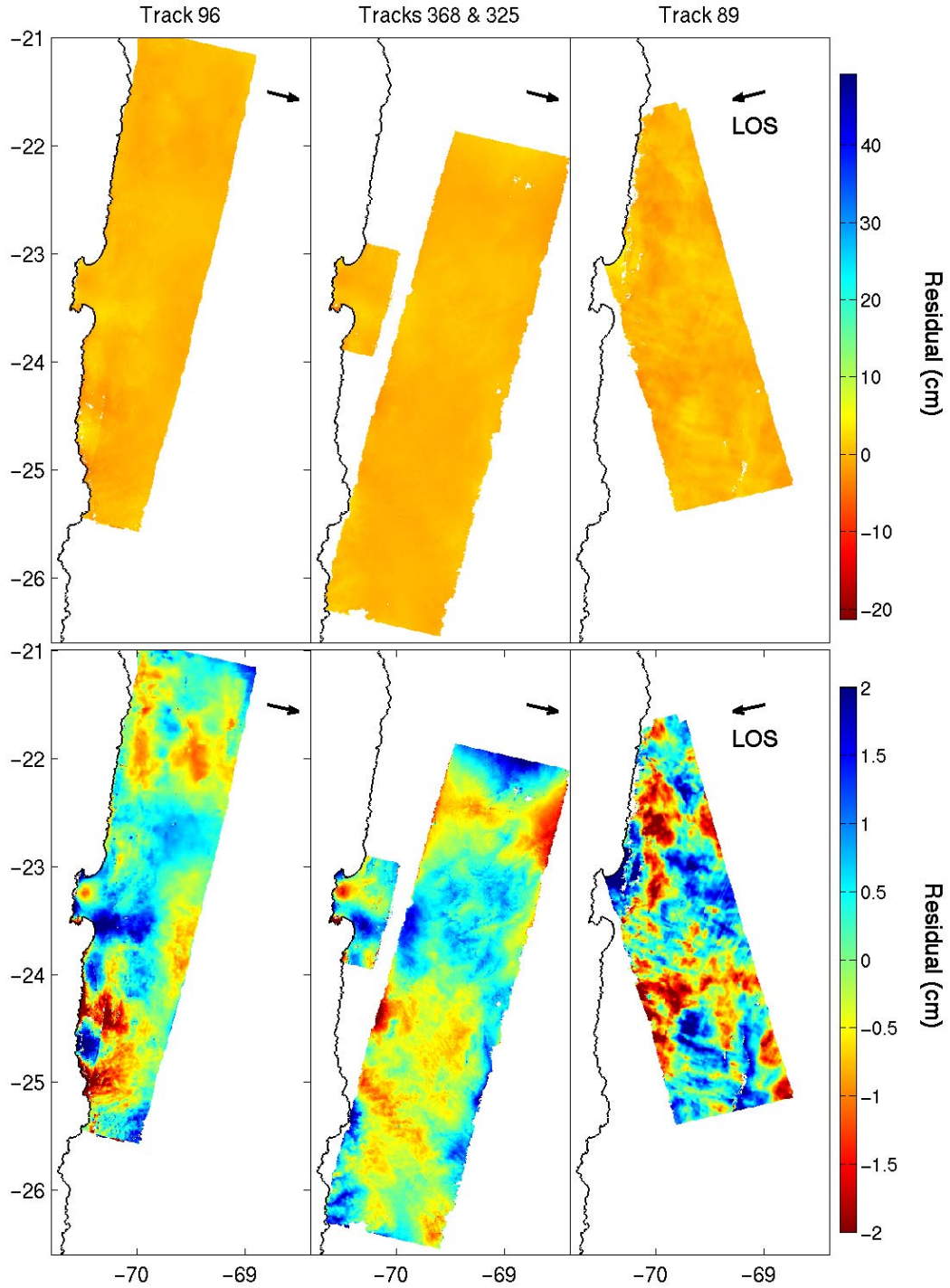


Figure 3.11: Residual of InSAR data from the preferred model for the four satellite tracks shown in Figure 3.5. The color scale used for displaying the data in Figure 3.5 is shown in the top row and an expanded color scale is used in the bottom row to show finer scale features. The RMS residual from the four InSAR tracks shown are: 0.69 cm for track 96, 0.58 cm for track 325, 0.87 cm for track 368, and 1.0 cm for track 89.

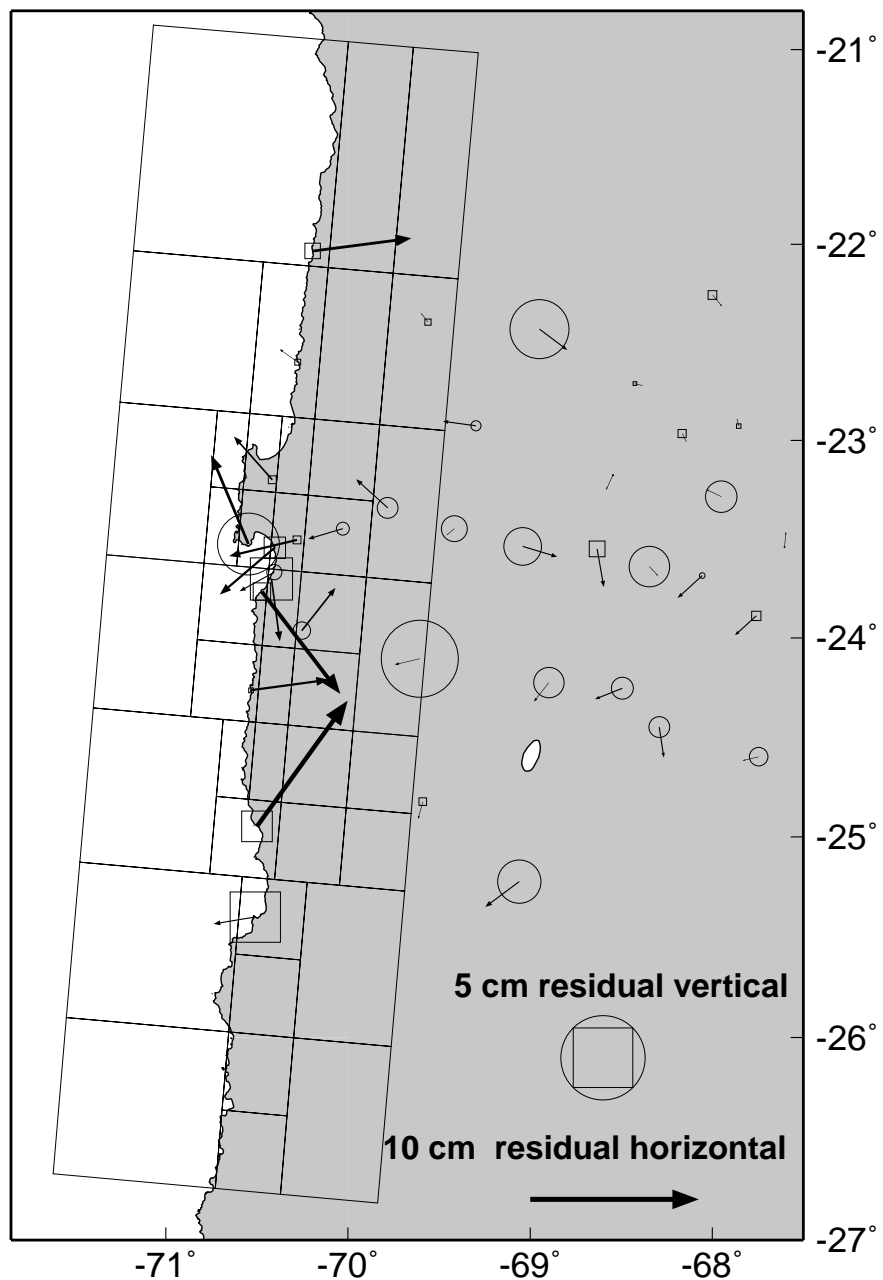


Figure 3.12: Residual displacements (data minus model) for the GPS data of *Klotz et al.* (1999). Horizontal residuals shown as arrows. Positive vertical residuals are circles and negative vertical residuals are squares. Using all stations, the RMS for east, north, and up are: 1.8, 1.8, and 1.7 cm, respectively, and total RMS for all components is 1.8 cm. If we consider only the 38 GPS stations shown in this figure the RMS for east, north, and up are: 2.3, 2.2, and 1.9 cm, respectively, and total RMS for all components is 2.1 cm.

mic – 1.6×10^{21} Nm (*Carlo et al.*, 1999), 1.5×10^{21} Nm (*Gouget et al.*, 1998), 1.2×10^{21} Nm (*Delouis et al.*, 1997), 0.9×10^{21} Nm (*Ruegg et al.*, 1996); seismic and GPS – 1.42×10^{21} Nm (*Ihmlé and Ruegg*, 1997); GPS – 1.78×10^{21} Nm (*Klotz et al.*, 1999), 1.5×10^{21} Nm (*Ruegg et al.*, 1996); coralline algae – 2×10^{21} Nm (*Ortlieb et al.*, 1996). Some of the spread in moment estimates can be explained by the different elastic structures used in the models (which vary from model to model by as much as 10%). However, some have argued that the discrepancy between the seismic moment inferred from geodesy and long period seismic waves is larger than body wave-based estimates (e.g., *Ruegg et al.*, 1996; *Delouis et al.*, 1997), possibly indicating significant moment release at low frequencies (*Ihmlé and Ruegg*, 1997; *Carlo et al.*, 1999).

We estimate rakes for the fault patches with the best constrained slip to lie between 92° and 136° (mean 113°) except for one patch (discussed below). Our estimated rake is close to the plate convergence direction of 103° (*DeMets et al.*, 1994) and consistent with 97° - 116° measured using a variety of techniques (*Carlo et al.*, 1999; *Ruegg et al.*, 1996; *Delouis et al.*, 1997; *Ihmlé and Ruegg*, 1997). The GPS-only inversion estimated the rake as 66° (*Klotz et al.*, 1999), which is 114° using our convention for rake direction. One patch at the south-east corner of the 1995 rupture area has a rake that is purely right-lateral. *Delouis et al.* (1997) fit a sub-event with a normal mechanism late in the rupture and *Carlo et al.* (1999) noted that this part of the rupture is difficult to fit with a thrust mechanism. We constrain our patches to slip in only a reverse and right-lateral sense, so we can not detect normal motion. The rake of this patch is very different from the others, indicating a possible local change in mechanism, but future joint geodetic and seismic inversions that allow for normal slip will be necessary to reconcile the datasets. This change in mechanism is spatially close to the location of possible triggered shallow slip of the Atacama fault (*Delouis et al.*, 1997; *Klotz et al.*, 1999), but the observations of surface rupture are ambiguous (*Ruegg et al.*, 1996; *Ortlieb et al.*, 1996).

Carlo et al. (1999) conclude that the 1995 earthquake was very smooth with no certain “asperities,” but with three areas of enhanced moment release. Although our

fault patches are large and do not resolve detailed structure, our slip distribution is relatively continuous and consistent with this result. We observe the maximum slip near the CMT location, as have others (*Carlo et al.*, 1999; *Delouis et al.*, 1997; *Klotz et al.*, 1999), and the magnitude (4 m) is within a range of previous estimates – 3.5 m (*Klotz et al.*, 1999) and 10 m (*Carlo et al.*, 1999). As with *Ihmlé and Ruegg* (1997), most of our slip is updip of the hypocenter and we do not have much slip between the hypocenter (NEIC location) and the CMT location ($\sim 30\%$), where the body-wave only inversions put 80% or more of the slip. *Ihmlé and Ruegg* (1997) attribute the difference in the location of moment release between the body wave and surface wave/geodetic studies to the fact that body wave only inversions do not approximate the rupture well.

The slip from the 1995 earthquake can be compared with the location of several M_w 7 earthquakes that occurred within the rupture area. Near the hypocenter of the M_w 7.5, 1987 earthquake, slip during the 1995 earthquake is primarily near the trench, while farther north, slip is closer to land. The seismic moment also decreases from north to south. Furthermore, our slip distribution indicates that the 1995 event had little slip near the rupture area of the 1988 M_w 7.2 earthquake. *Ihmlé and Ruegg* (1997) and *Delouis et al.* (1997) explain these observations as due to the prior release of slip from the 1987 event, which must have been concentrated near the hypocenter, since the Harvard CMT location lies well updip in the an area of high slip during the 1995 event. Alternatively, the absence of slip near the locations of the 1987 and 1988 events could be due to aseismic slip, or the slip deficit could be released in a future event (*Carlo et al.*, 1999). A preliminary inversion of an interferogram from the M_w 7.1 1998 event indicates that most of its slip was in a region of low slip during the 1995 earthquake, and down-dip of an area of large slip in the 1995 event (see Chapter 4).

3.5.2 Comparison with other measurements

To understand how the different datasets used in the inversion contribute to the estimation and resolution of slip, we conduct three separate inversions: one with only GPS data, one with only InSAR data from descending orbits only, and one with all available InSAR data. Not surprisingly, inversions with only GPS data best resolve the slip near where there are GPS benchmarks (Figure 3.13, upper left). Predicted interferograms made with the GPS-only model are very different (10's of cm) from the observed LOS displacements in areas where there are no GPS benchmarks (Figure 3.13). The model patches near the trench can cause more horizontal than vertical deformation on land, and because GPS data are more sensitive than InSAR to the horizontal component, the former better resolve slip near the trench. However, when both ascending and descending InSAR data are used, the model resolution near the trench is nearly the same as the GPS resolution of those patches, and illustrates the importance of acquiring both ascending and descending data.

Our resolution tests also show that addition of a single frame from track 368 and the addition of multiple interferograms spanning different time intervals also aid in model resolution, although the ascending track contributes the most. The combined GPS and InSAR resolution of these patches (Figure 3.8) is higher than the resolution of either independent data set, as found for the 1992 Landers, California, strike-slip earthquake (*Hernandez et al.*, 1999). The synergistic combination of GPS and InSAR becomes less important when we consider all possible InSAR data. We did not use the single frame of data from track 361 (the ascending track immediately south of track 89) in our inversions, but when we include synthetic data from this track in our SAR only model resolution tests, the resolution is comparable to the combined InSAR/GPS resolution. This further illustrates the importance of collecting both ascending and descending orbits, and indicates that in some locations, remote sensing SAR data alone can resolve model parameters as well as data acquired on the ground with sparse GPS arrays.

The GPS and InSAR measurements of deformation can be directly compared

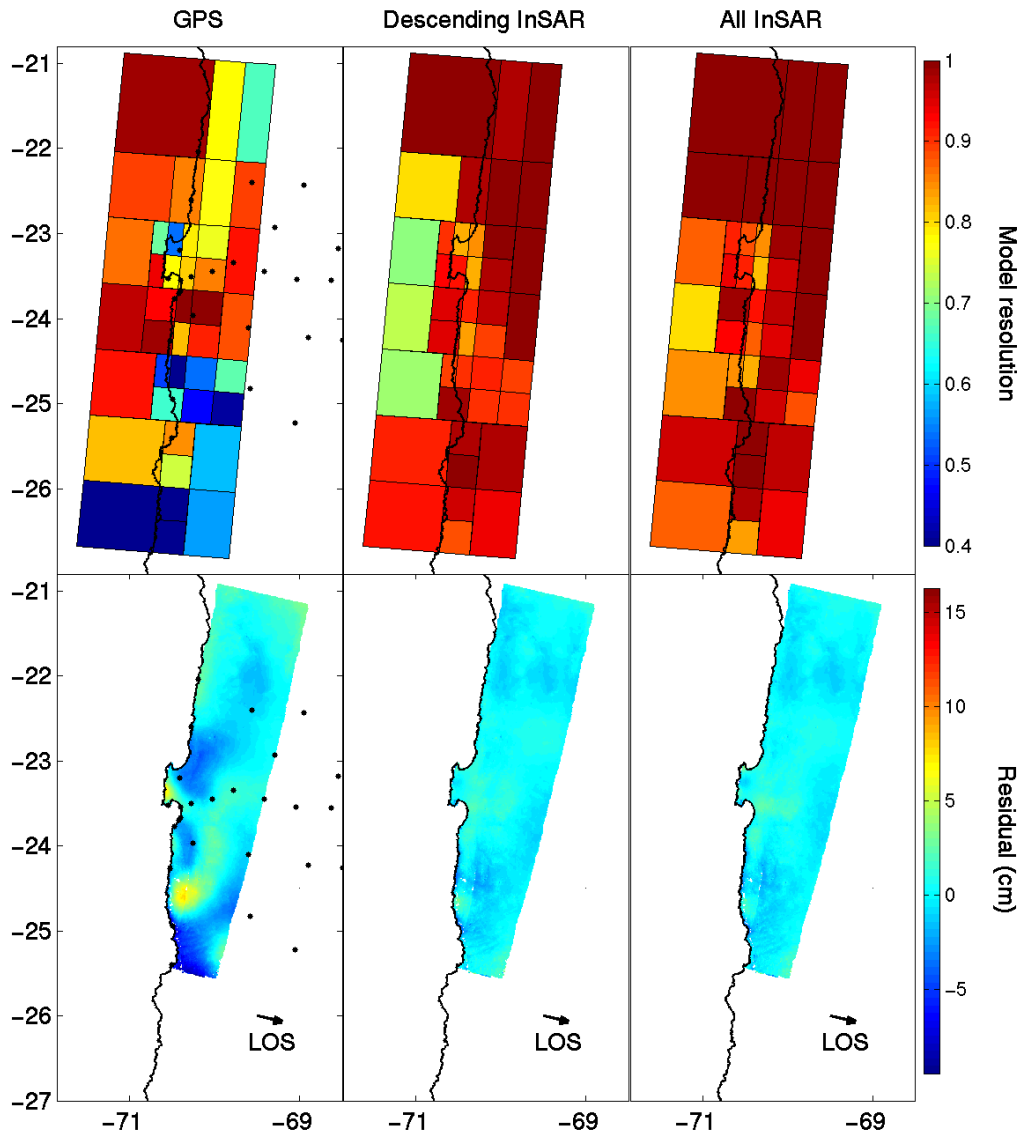


Figure 3.13: Comparison between model resolution and the difference between observed and predicted interferograms for inversions that used only the GPS data (top) only descending InSAR data (middle) and ascending and descending InSAR data (bottom). The residual from the interferogram spanning 5/8/1992-10/9/1995 from track 96 is shown, since this span includes the most GPS points and most closely matches the interval over which the GPS data were collected. The black dots on the two leftmost figures show the location of the GPS stations.

when the GPS station lies within a part of the interferogram that was successfully unwrapped (Figure 3.14). The GPS data were projected into the radar LOS and both the GPS and InSAR raw data were corrected by the best-fit quadratic ramp calculated during the inversion of co-seismic slip. The quadratic ramp independently corrects for any potential inter-seismic slip in both the InSAR and GPS (because they span different time periods) and systematic InSAR orbital errors. The RMS error for 90 point comparisons between InSAR and GPS in the nine interferograms is 3.2 cm, which is larger than the vertical GPS error of about 5 mm (*Klotz et al.*, 1999), which dominates the error estimate because of the steep incidence angle, but is comparable with results at other earthquakes. The estimated 5 mm vertical error is probably optimistic for campaign GPS measurements. Published RMS differences between InSAR and GPS measurements from the 1992 Landers, California earthquake are 3.4 cm for 9 points (*Massonnet et al.*, 1993), 11 cm for 19 points (*Massonnet and Feigl*, 1998) and 18.9 cm for 18 points (*Zebker et al.*, 1994), 1.6 cm for 7 points for the 1994 Northridge, California, earthquake, and for the 1999 Hector Mine, California, earthquake: about 4.9 cm in the LOS (*Jónsson et al.*, 2002) or between 4.9 cm and 20.5 cm in the east and north components (*Fialko et al.*, 2001b).

We compare the uplift of coralline algae at 27 points along the coast measured by *Ortlieb et al.* (1996), and revised by Ortlieb (personal communication, 2000), with the predicted uplift from our preferred model (Figure 3.15). The RMS difference is 10.9 cm. The largest discrepancy is at the point of maximum uplift (0.8 m), near Punta Tetas, where the predicted value more closely matches the preliminary estimate (*Ortlieb et al.*, 1995) than the final one, although *Ortlieb et al.* (1996) discusses why the precision of this measurement might be poor. *Ortlieb et al.* (1996) states that some localized tectonic motion might be necessary to account for the observed uplift at the southernmost point (Punta Tragagente), since there is no observed uplift along the coast to the immediate north or south. We do not see any evidence for such localized deformation in the interferograms, although such motion might be hard to detect, since in general, the correlation of the images decreases near the coast.

We compare the observed interferograms with those predicted from the models

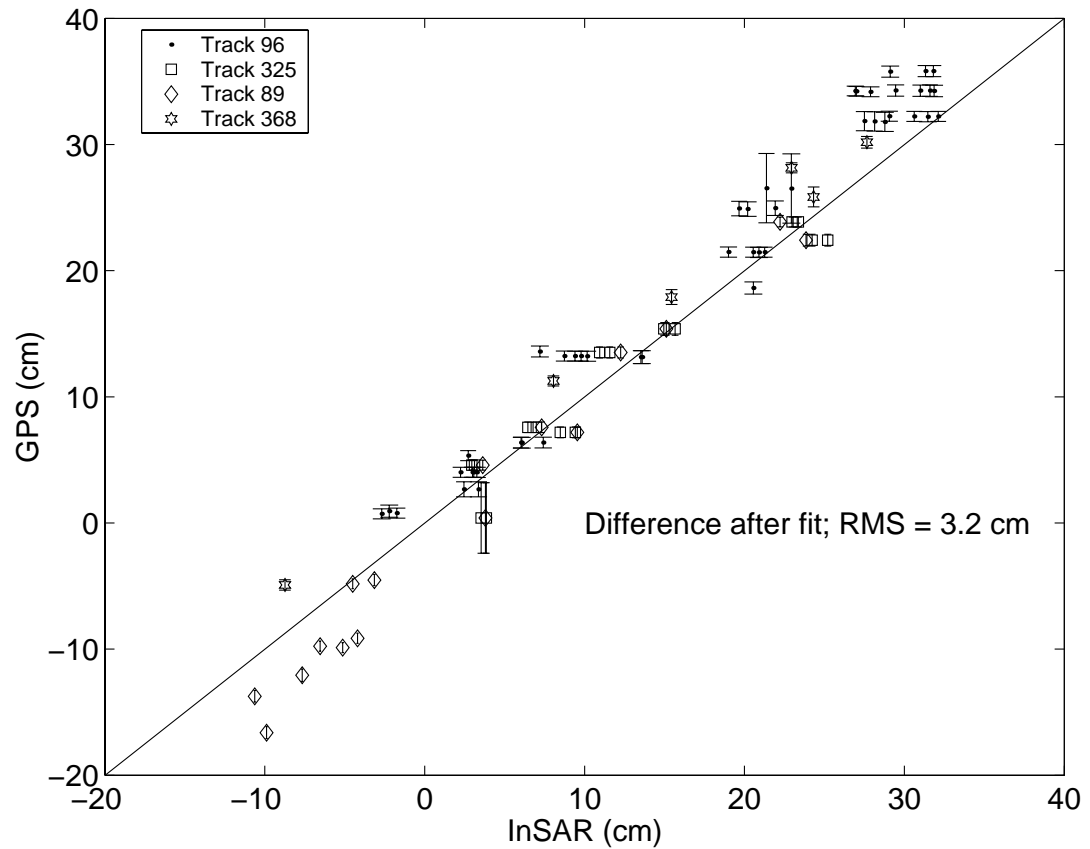


Figure 3.14: Comparison between 90 GPS displacements (*Klotz et al.*, 1999) projected in the radar LOS and InSAR observations for the four satellite tracks. The independently determined best-fit quadratic ramp from our preferred co-seismic model has been removed from the GPS and InSAR data. The RMS difference is 3.2 cm.

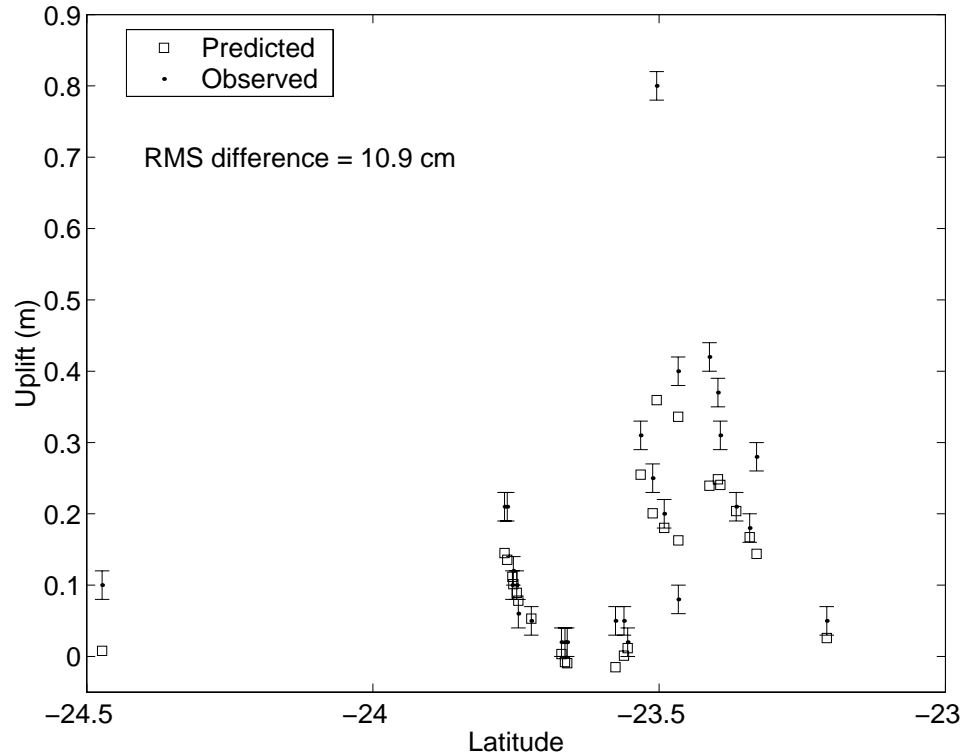


Figure 3.15: Comparison between our preferred co-seismic surface displacement model (squares) and the observed coast coralline algae uplift (dots) of *Ortlieb et al.* (1996), as revised by Ortlieb (personal communication, 2000). The RMS difference is 10.9 cm, but if we remove the data point with the largest residual, the RMS difference is 6.8 cm. *Ortlieb et al.* (1996) do not specify errors for each measurement, but estimate an overall precision of 2 cm, shown as the error bars.

of Ruegg *et al.* (1996) and Ihmlé and Ruegg (1997) (shown wrapped in Figure 3.16 and unwrapped in Figure 3.17). The model of Ruegg *et al.* (1996) is a three point source model derived from inversions of teleseismic body waves which explains the main features of the source time function, but poorly estimates the surface displacement. In particular, the region of uplift on the Mejillones Peninsula appears shifted to the north compared to our observations or the model of Ihmlé and Ruegg (1997). In a study of the induced tsunami, Guibourg *et al.* (1997) needed to shift the single patch of the Ruegg *et al.* (1996) displacement model to match the tide-gauge record at Antofagasta, but found that the variable slip model of Ihmlé and Ruegg (1997) adequately matches the gauge record. Ihmlé and Ruegg (1997) used both teleseismic Rayleigh waves and static displacements measured by 10 GPS stations to constrain the slip on the fault plane. The difference between their predicted LOS displacements and the observed interferogram are large (10's of cm) in places, although the difference is less near the locations of the GPS stations. Hernandez *et al.* (1997) compared synthetic interferograms generated with seismological models of slip from the 1992 Landers, California earthquake with observed interferograms. They found good agreement between the predicted and observed interferograms (cm scale residual) except in regions within 7 km of the fault where they thought that the model fault parameterization might be too crude and the unwrapping of the observed interferogram might not be reliable. The fact that the seismic prediction at Landers more closely matches the observations than at Chile might be related to the fact that the Landers seismic inversion used local strong-motion data while the Chile seismic inversion relied upon teleseismic data.

3.6 Summary

We have used two techniques to invert nine interferograms and GPS data spanning the 1995, M_w 8.1 Antofagasta, Chile, earthquake for slip along the subduction zone interface. We favor the constrained least squares (CLS) inversion over the singular value decomposition (SVD) because CLS resolves model parameters and has a result

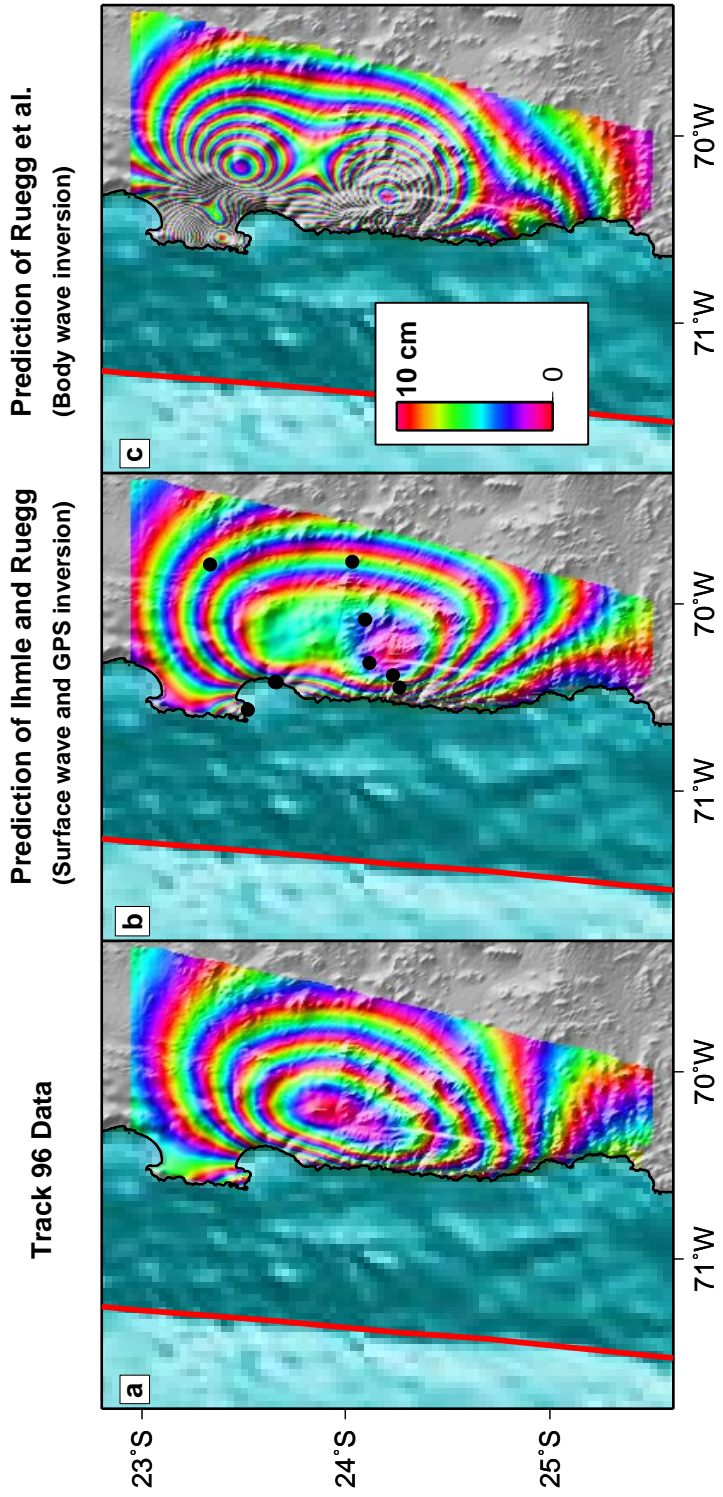


Figure 3.16: Comparison of actual (a.) and predicted LOS displacements for track 96 from the models of *Ihmle and Ruegg* (1997) (b.) and *Ruegg et al.* (1996) (c.). The black dots in the center show the GPS stations used in the inversion of *Ihmle and Ruegg* (1997).

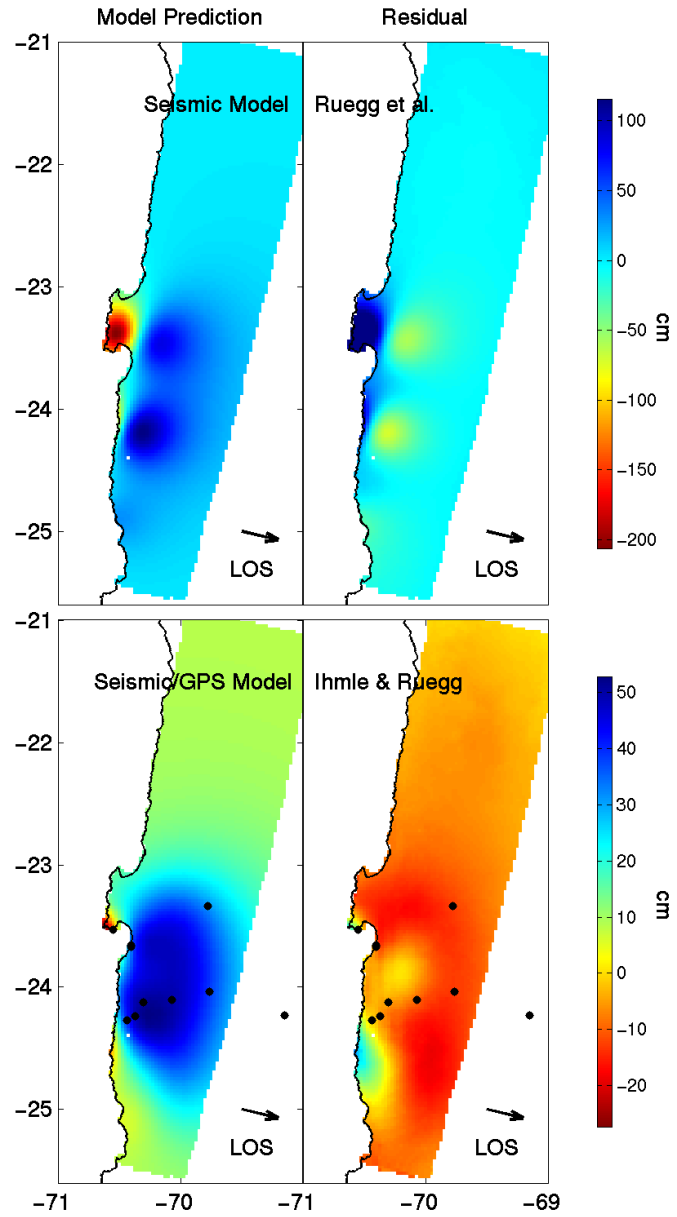


Figure 3.17: Predicted LOS displacements for track 96 from the models of Ruegg *et al.* (1996) (top left) and Ihmlé and Ruegg (1997) (bottom left) and the difference between the observations from the track 96 co-seismic pair and the prediction (top right and bottom right, respectively). The best-fitting quadratic ramp derived from our modeling was removed from the interferogram for the sake of comparison. The model of Ruegg *et al.* (1996) is a three point source model made from inversions of teleseismic body waves while the model of Ihmlé and Ruegg (1997) uses both teleseismic Rayleigh waves and 10 GPS stations (shown in black dots).

that is more consistent (in terms of moment and rake) with previous geodetic and seismic inversions of slip. Our slip model shows an absence of slip near the location of several M_w 7 earthquakes within the rupture area. Tests of the sensitivity to the inclusion of different subsets of the InSAR and GPS data demonstrate that the GPS data alone does not completely characterize surface deformation and that InSAR data from many different viewing geometries is necessary to maximize resolution. The difference between the GPS data projected into the radar LOS and the InSAR data is reasonable (about 3 cm) considering the long time periods spanned by both data sets and our simple removal of potential inter- and post-seismic deformation by fitting for quadratic ramps. The difference between our model of co-seismic uplift and observations of coralline algae uplift (*Ortlieb et al.*, 1996) is 10 cm – we do not understand why this difference is so large. Predicted LOS displacements from seismic (*Ruegg et al.*, 1996) and seismic/geodetic (*Ihmlé and Ruegg*, 1997) models differ from observed interferograms by 10's of cm. The discrepancy between the predicted LOS displacement from the model of *Ihmlé and Ruegg* (1997) and the observed interferograms is surprising considering the many similarities between their slip distribution and ours (see above). A complete joint InSAR/GPS/seismic inversion is necessary (see Chapter 4). A joint inversion will also test for a change in focal mechanism in the southeast portion of the rupture which we and others observe (*Delouis et al.*, 1997; *Carlo et al.*, 1999). As *Carlo et al.* (1999) and others have noted, there is no obvious relation between the distribution of aftershocks and slip. It might be that the aftershock distribution is more correlated to stresses induced by post-seismic than co-seismic deformation as is suggested for the 1994 Northridge earthquake (*Deng et al.*, 1999). Post-seismic deformation is expected in the area since the co-seismic deformation is opposite long-term tectonic deformation in most places (*Delouis et al.*, 1998), and is observed by GPS (*Klotz et al.*, 2000).